materials

MDPI

Article

Oxygen-Plasma-Induced Hetero-Interface $NiFe_2O_4/NiMoO_4$ Catalyst for Enhanced Electrochemical Oxygen Evolution

Nuo Xu [1,†], Wei Peng [2,†], Lei Lv [2], Peng Xu [2], Chenxu Wang [1], Jiantao Li [3], Wen Luo [1,2,*] and Liang Zhou [2]

[1] Department of Physics, School of Science, Wuhan University of Technology, Wuhan 430070, China; mr.promise@whut.edu.cn (N.X.); 245856@whut.edu.cn (C.W.)
[2] State Key Laboratory of Advanced Technology for Materials Synthesis and Processing, Wuhan University of Technology, Wuhan 430070, China; pw0225@whut.edu.cn (W.P.); lvlei1028@whut.edu.cn (L.L.); xupeng620@whut.edu.cn (P.X.); liangzhou@whut.edu.cn (L.Z.)
[3] Chemical Sciences and Engineering Division, Argonne National Laboratory, Lemont, IL 60439, USA; jiantao_work@126.com
* Correspondence: luowen_1991@whut.edu.cn
† These authors contributed equally to this work.

Abstract: The electrolysis of water to produce hydrogen is an effective method for solving the rapid consumption of fossil fuel resources and the problem of global warming. The key to its success is to design an oxygen evolution reaction (OER) electrocatalyst with efficient conversion and reliable stability. Interface engineering is one of the most effective approaches for adjusting local electronic configurations. Adding other metal elements is also an effective way to enrich active sites and improve catalytic activity. Herein, high-valence iron in a heterogeneous interface of $NiFe_2O_4/NiMoO_4$ composite was obtained through oxygen plasma to achieve excellent electrocatalytic activity and stability. In particular, 270 mV of overpotential is required to reach a current density of 50 mA cm^{-2}, and the overpotential required to reach 500 mA cm^{-2} is only 309 mV. The electron transfer effect for high-valence iron was determined by X-ray photoelectron spectroscopy (XPS). The fast and irreversible reconstruction and the true active species in the catalytic process were identified by in situ Raman, ex situ XPS, and ex situ transmission electron microscopy (TEM) measurements. This work provides a feasible design guideline to modify electronic structures, promote a metal to an active oxidation state, and thus develop an electrocatalyst with enhanced OER performance.

Keywords: hetero-interface; oxygen plasma; oxygen evolution reaction; electrocatalysis; electronic modulation

check for updates

Citation: Xu, N.; Peng, W.; Lv, L.; Xu, P.; Wang, C.; Li, J.; Luo, W.; Zhou, L. Oxygen-Plasma-Induced Hetero-Interface $NiFe_2O_4/NiMoO_4$ Catalyst for Enhanced Electrochemical Oxygen Evolution. *Materials* **2022**, *15*, 3688. https://doi.org/10.3390/ma15103688

Academic Editors: Fernando B. Naranjo and Susana Fernández

Received: 24 April 2022
Accepted: 18 May 2022
Published: 20 May 2022

Publisher's Note: MDPI stays neutral with regard to jurisdictional claims in published maps and institutional affiliations.

Copyright: © 2022 by the authors. Licensee MDPI, Basel, Switzerland. This article is an open access article distributed under the terms and conditions of the Creative Commons Attribution (CC BY) license (https://creativecommons.org/licenses/by/4.0/).

1. Introduction

Nowadays, the dramatically increased demand for fossil energy has resulted in the depletion of traditional energy materials and has generated concerns regarding energy security and the environmental pollution caused by the extensive use of fossil energy [1]. Overall, water electrolysis has developed as an ideal and effective approach for producing hydrogen, an alternative clean energy source to traditional fossil fuels [2,3]. The oxygen evolution reaction (OER) involves multiple steps of proton coupling and a complex four-electron transfer process [4–6]. The sluggish reaction kinetics eventually cause a high enough overpotential to trigger the OER, which is a key factor limiting the efficiency of water electrolysis [3,7]. To date, the most effective catalysts for the OER have been found to be rare metal oxides, such as IrO_2 and RuO_2, as they significantly reduce the overpotential required for the OER. However, the high expenditure and scarcity of precious metals restrict their wide application for practical industrialization as efficient electrocatalysts.

Due to the abundant transition metal resources of the Earth itself, the construction of non-noble metal OER electrocatalysts has received much attention recently [6,8–10]. This includes transition metal compounds based on nickel, iron, or cobalt (Ni, Fe, and Co nonoxides [11–14]; oxides [15–18]; hydroxides [19–21]; and oxyhydroxides [22–25]), which have

shown high conversion efficiencies towards the OER as substitutes for a precious metal electrocatalyst. Meanwhile, growing nanostructured catalysts directly on conductive substrates, such as Ni foam, has been established to decrease contact resistance and effectively improve energy efficiency [26–28]. Among these transition metal compounds, $NiMoO_4$ on Ni foam has been researched as a promising electrocatalyst for its facile synthesis in large quantities. However, its intrinsic activity still remains defective, especially for its deficient active site (only Ni site) [29–32].

Generally, it is crucial to consider the modification of structure and electronic configuration in order to achieve outstanding OER performance, especially in order to attain a higher current at a lower overpotential with long-term stability [5]. An atomic-scale approach for constructing a reliable interface, especially a hetero-interface between different nanomaterials, has been intensively adopted to modify the local electronic structure of materials [33]. This approach can accelerate the reaction kinetics by combining the structural advantages of each component, thus improving the catalytic performance of nanocomposites [34–38]. For example, Lv et al. synthesized a core–shell structure of NiFe-60/Co_3O_4 on Ni Foam with an obvious and clear hetero-interface between the Co_3O_4 nanowire and the NiFe-layered double hydroxide nanosheet [39]. A hetero-interface contributes to the interaction between two different nanomaterials, facilitates electron transfer, and further leads to enhanced catalytic activity for the OER. Zhang et al. demonstrated a CoN_4-based metal−organic framework (MOF) with embedded $CoFeO_x$ nanoparticles; Co sites anchoring on the $CoFeO_x$/MOF interface brought about an altered 3D electronic configuration for the interfacial Co and a higher valence [40]. In addition, composites consisting of multivariate transition metals can promote the exceptional modification of active sites within the matrix, and thus improve reaction efficiency and durability [41]. Based on this, the addition of Fe elements has been confirmed as a proper approach to enrich the active sites and boost highly efficient OER performance [42–44].

Herein, we report a hetero-interface made of $NiFe_2O_4$ nanoparticles (NPs) and a $NiMoO_4$ nanowire (denoted as $NiFe_2O_4/NiMoO_4$). Briefly, $NiMoO_4$ nanowires were prepared on nickel foam through a facile hydrothermal synthesis. NiFe Prussian blue analogs (NiFe PBA) were firstly fixed on the $NiMoO_4$ nanowires by iron exchange. Then, oxygen (O_2) plasma converted the NiFe PBA to $NiFe_2O_4$ to form a $NiFe_2O_4/NiMoO_4$ hetero-interface. As-synthesized, the $NiFe_2O_4/NiMoO_4$ exhibits excellent performance for the OER with a low overpotential of 309 mV required to reach 500 mA cm^{-2} and a satisfactory stability (a 4% increase in the overpotential at 50 mA cm^{-2} over 150 h). The shift in the binding energy of metal sites increased the electronic interaction of the modulated hetero-interface. To understand its excellent OER performance, in situ Raman measurements, ex situ transmission electron microscopy (TEM), and ex situ X-ray photoelectron spectroscopy (XPS) were used to confirm the fast and irreversible reconstruction and identify the true active species in the catalytic process.

2. Results and Discussion

The schematics shown in Figure 1a illustrate the preparation of $NiFe_2O_4$ nanoparticles integrated with $NiMoO_4$ nanowires on nickel foam. Briefly, through a simple hydrothermal method [45], hydrated $NiMoO_4$ nanowires were vertically germinated on Ni foam. In accordance with a previous report [46], the NiFe PBA was grown on $NiMoO_4$ nanowires and the MoO_4^{2-} on the surface of the nanowires was replaced with K^+ and $[Fe(CN)_6]^{3+}$ by ion exchange. The NiFe PBA on the $NiMoO_4$ surface was converted to $NiFe_2O_4$ NPs under O_2 plasma treatment, and $NiFe_2O_4/NiMoO_4$ was obtained. For comparison, $NiMoO_4$ nanowires were also placed under the same O_2 plasma treatment and denoted as $NiMoO_4$ O_2-Pl.

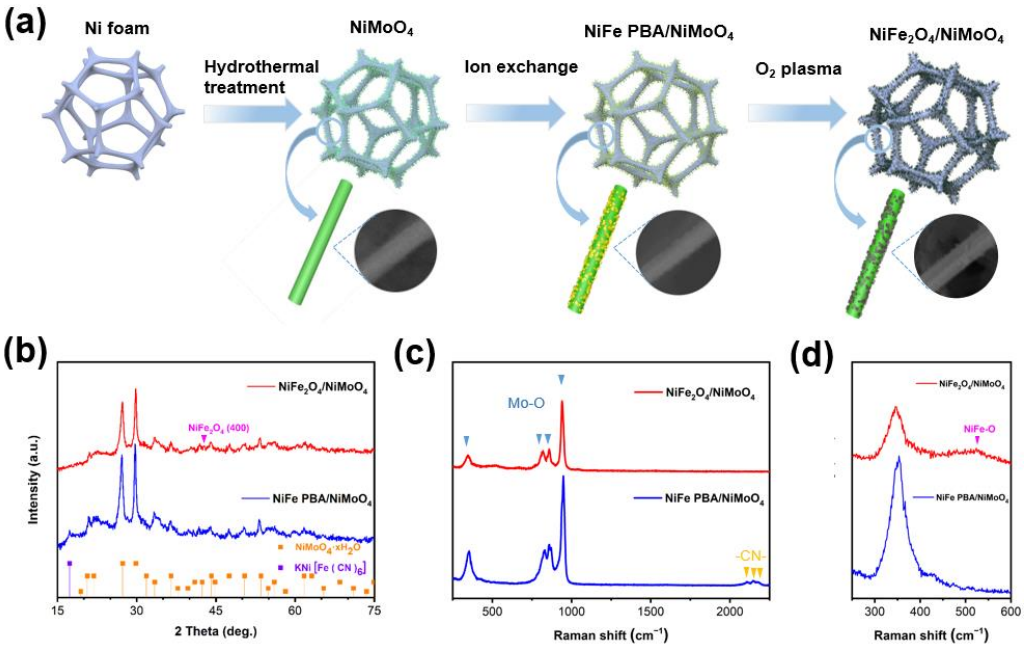

Figure 1. (**a**) Schematic illustration of the synthesis of $NiFe_2O_4/NiMoO_4$; (**b**) XRD patterns of NiFe PBA/$NiMoO_4$ and $NiFe_2O_4/NiMoO_4$; (**c**) Raman spectra of NiFe PBA/$NiMoO_4$ and $NiFe_2O_4/NiMoO_4$; and (**d**) Raman spectra of NiFe PBA/$NiMoO_4$ and $NiFe_2O_4/NiMoO_4$ in a region from 250 cm^{-1} to 750 cm^{-1}, respectively.

Characterization of $NiMoO_4$. Figure S1a,b indicate that the $NiMoO_4$ possessed an even and well-defined nanowire morphology. Its average diameter was about 100 nm. As the XRD patterns show in Figure S2a, the diffraction peaks of the $NiMoO_4$ were in perfect agreement with the $NiMoO_4 \cdot xH_2O$ (JCPDF: 00-013-0128), which means the $NiMoO_4 \cdot xH_2O$ was highly crystalline. In the FT-IR spectra shown in Figure S3, the two peaks at 1628 and 3446 cm^{-1} correspond to the stretching vibration of hydroxyl (-OH), which can be ascribed to the bending mode of crystal water in the $NiMoO_4 \cdot xH_2O$ and the surface-adsorbed water molecules [47].

Characterization of NiFe PBA/$NiMoO_4$. As shown in Figure 1b, a weak diffraction peak appears at 17.3°, which can be attributed to the $KNi[Fe(CN)_6]$ (JCPDF: 01-089-8978). At the same time, the diffraction peaks of the $NiMoO_4 \cdot xH_2O$ still remain in the NiFe PBA/$NiMoO_4$. In Figure S1c,d, the surface of the $NiMoO_4$ nanowires is covered with small-sized NiFe PBA NPs, indicating the expected process of the iron exchange. Figure 1c reveals peaks at 357, 828, 872, and 950 cm^{-1} for the NiFe PBA/$NiMoO_4$, which can be assigned to the Mo-O vibration, and this result is consistent with previous reports [32]. In addition, the NiFe PBA/$NiMoO_4$ exhibits three peaks around 2100 cm^{-1}, which can be attributed to -CN [48,49]. In Figure S3, for the NiFe PBA/$NiMoO_4$, a new characteristic peak can be observed at 2099 cm^{-1} in the FT-IR spectrum, which is attributed to the stretching vibrations of -CN in the NiFe PBA NPs [50]. In Figure S5a, for the NiFe PBA/$NiMoO_4$, the Ni 2p spectra can be deconvoluted into four peaks and two wide satellite peaks. In the Ni $2p_{3/2}$, the peaks at 856.2 eV and 857 eV can be ascribed to the Ni^{2+} and Ni^{3+} species, respectively. Meanwhile, in the Ni $2p_{1/2}$, the peaks of the Ni^{2+} and Ni^{3+} species can be fitted at 874.0 eV and 875.2 eV, respectively. In addition, two satellite peaks for Ni can be observed at 862.8 and 880.7 eV [51]. As shown in Figure S5b, the further fitted peaks at 708.5 and 709.1 eV in the Fe $2p_{3/2}$ are ascribed to Fe^{2+} and Fe^{3+}, respectively, while the peaks observed at 721.6 and 722.2 eV in the Fe $2p_{1/2}$ are owed to the existence of Fe^{2+} and Fe^{3+}, respectively. The ratio of the Fe^{3+} to Fe^{2+} peak areas in the Fe $2p_{3/2}$ was calculated as 0.948. Furthermore, one satellite peak for Fe appears at 715.7 eV [51].

Characterization of $NiFe_2O_4/NiMoO_4$. In Figure 1b, compared to the NiFe PBA/$NiMoO_4$, the diffraction peak initially attributed to $KNi[Fe(CN)_6]$ disappears, and a new weak diffraction

peak can be observed at 43.3°, which is attributed to the (400) planes of the $NiFe_2O_4$ (JCPDS: 44-1485). As shown in Figure 1c, the characteristic Raman peaks attributed to the Mo-O bond still remain, while the peak owed to -CN disappears. A broad peak at 520 cm^{-1} in Figure S2b indicates the formation of NiFe-O. The same phenomenon is shown in Figure S3, as the characteristic peak of -C≡N- disappears and an apparent peak at 1384 cm^{-1} can be assigned to the C=O in CO_2 and the stretching vibration of the interlayer $NO_3^=$ groups [47]. This is related to the decomposition of PBA under O_2 plasma treatment. As shown in Figure 2a, the $NiMoO_4$ remains in the structure of the nanowire with a diameter of 100 nm, similarly to the $NiMoO_4$ and NiFe PBA/$NiMoO_4$, while the $NiFe_2O_4$ nanoparticles slightly agglomerate. The TEM image of the $NiFe_2O_4/NiMoO_4$ (Figure 2b) clearly shows the $NiFe_2O_4$ NPs anchoring on the surface of the $NiMoO_4$ nanowire. The high-resolution transmission electron microscope (HRTEM) image in Figure 2c indicates the high-crystalline characteristic of the $NiMoO_4$. The HRTEM image in Figure 2d shows the apparent hetero-interface of the $NiFe_2O_4/NiMoO_4$. The lattice spacing of 2.08 Å can be attributed to the (400) plane of the $NiFe_2O_4$ and the lattice spacing of 3.26 Å assigned to the $NiMoO_4 \cdot xH_2O$. The elemental mapping images (Figure 2e) indicate that the Fe element is evenly distributed on the $NiMoO_4$ nanowires in the form of nanoparticles. Table S1 shows the chemical composition of the $NiFe_2O_4/NiMoO_4$. The molecular ratio of $NiFe_2O_4$ and $NiMoO_4$ in the $NiFe_2O_4/NiMoO_4$ is 1:17.27.

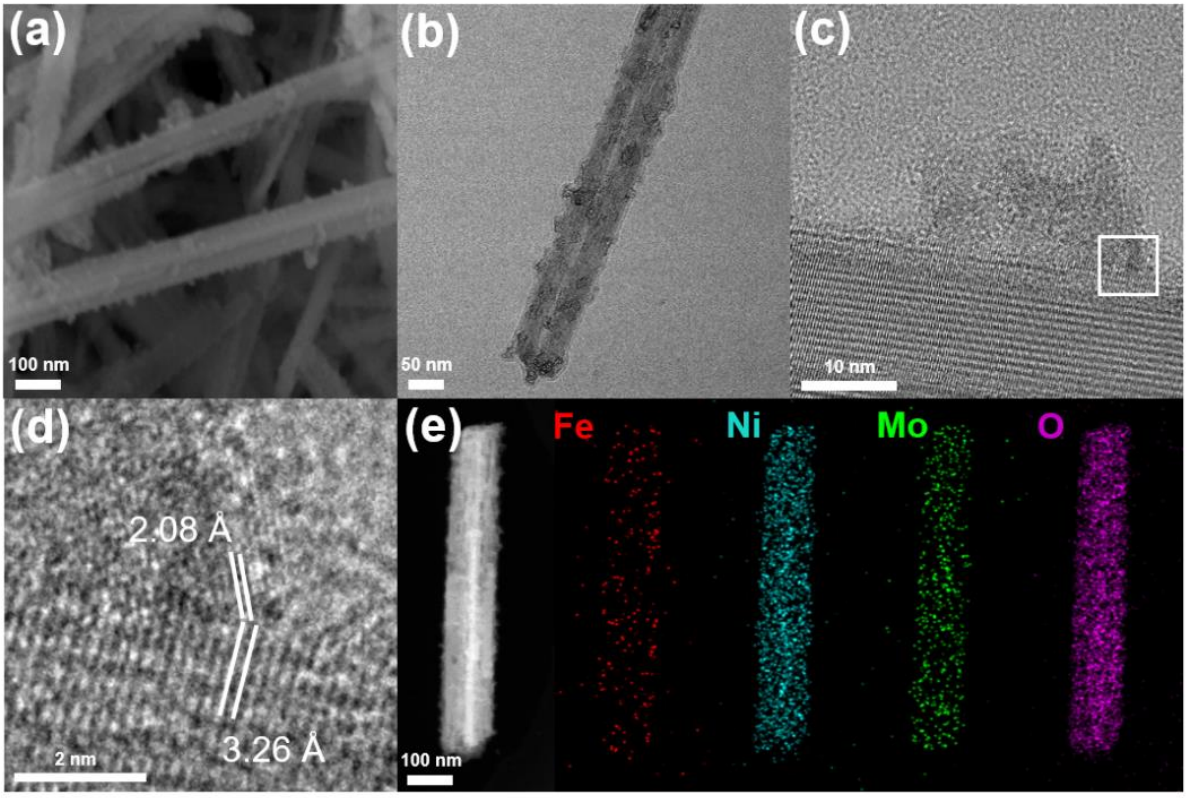

Figure 2. (**a**) SEM image, (**b**) TEM image, and (**c**) HRTEM images of $NiFe_2O_4/NiMoO_4$; (**d**) the corresponding HRTEM images of selected areas; and (**e**) EDS mapping images for Fe, Ni, Mo, and O elements of $NiFe_2O_4/NiMoO_4$.

XPS was used to analyze and further explore the surface electronic interaction of the $NiFe_2O_4/NiMoO_4$. The Ni 2p spectra of $NiFe_2O_4/NiMoO_4$ contain four fitted peaks with wide satellites (Figure 3a). The fitted peaks at 856.1 and 873.7 eV in the Ni $2p_{3/2}$ and the Ni $2p_{1/2}$, respectively, can be attributed to Ni^{2+}, while another two peaks (858.3 and 875.9 eV) correspond to the Ni^{3+} species. The wide peaks observed at 862.3 and 879.9 eV are owed to the satellites of Ni [52]. As Figure 3b shows, the fitted peaks at 710.7 and 713.3 eV can be related to Fe^{2+} and Fe^{3+} in the Fe $2p_{3/2}$, and the same is true for another two peaks

at 723.8 and 726.4 eV in the Fe $2p_{1/2}$ [53]. The broad peaks at 718.8 and 731.9 eV can be attributed to the satellite peaks of Fe. In Figure S6a,b, the peaks in the Ni $2p_{3/2}$ and the Mo 3D of the $NiFe_2O_4/NiMoO_4$ exhibit slightly negative shifts of about 0.2 eV compared with those observed from the spectra of the NiFe PBA/$NiMoO_4$. The peaks of the Fe 2p exhibit a distinct positive shift compared with those of the NiFe PBA/$NiMoO_4$, and the ratio of the Fe^{3+} to Fe^{2+} peak area in the Fe $2p_{3/2}$ (Figures S5b and 3b) increases from 0.948 in the NiFe PBA/$NiMoO_4$ to 1.706 in the $NiFe_2O_4/NiMoO_4$. The negative movement of binding Ni and Mo energy indicates the regulation of the electronic structure in the hetero-interface. Meanwhile, oxygen plasma leads to the oxidation of Fe, and these two factors eventually promote an increase in the binding energy of Fe. It has been confirmed that Fe with a high valence state promotes processes in the OER [54–56]. The fitted O 1s peaks at 530.7, 532.3, and 533.3 eV can be attributed to metal-O, C=O [57], and surface-adsorbed oxygen, respectively.

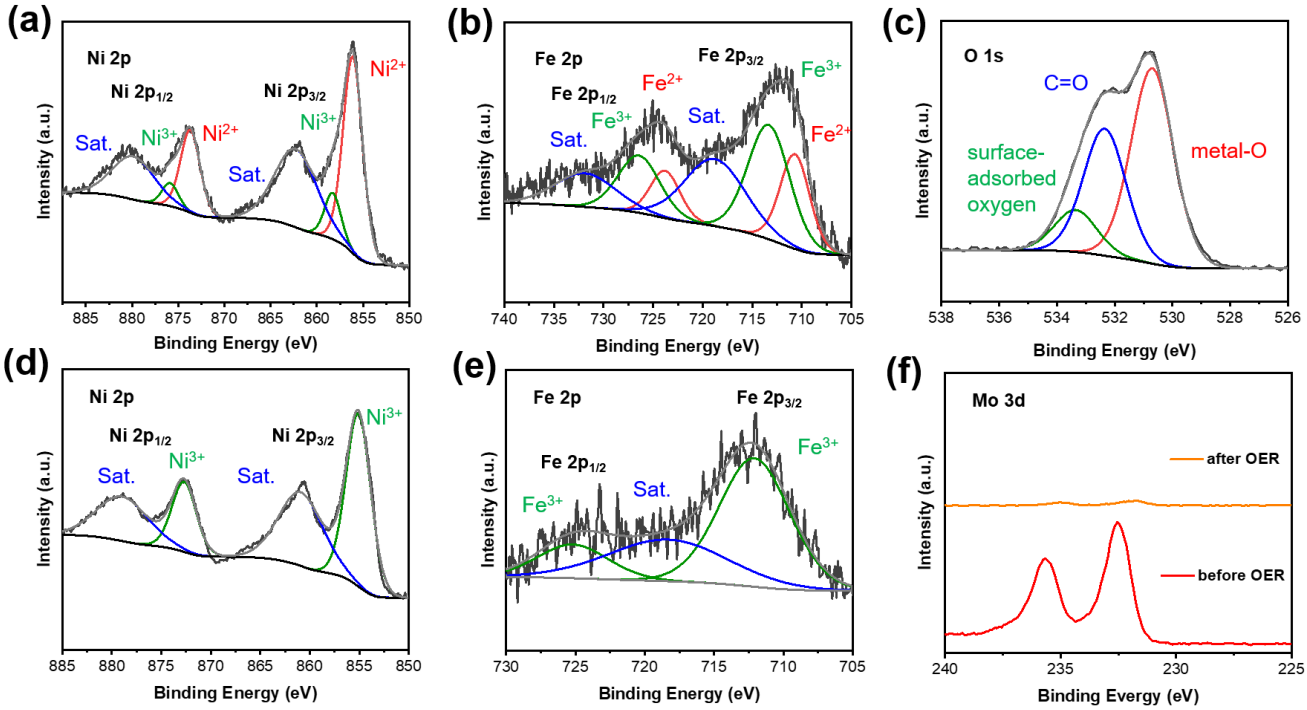

Figure 3. XPS: (**a**) Ni 2p, (**b**) Fe 2p, and (**c**) O 1s spectra of $NiFe_2O_4/NiMoO_4$; (**d**) Ni 2p and (**e**) Fe 2p spectra of $NiFe_2O_4/NiMoO_4$ after OER testing for 3 h; (**f**) Mo 3D spectra of $NiFe_2O_4/NiMoO_4$ before OER testing and after OER testing.

Electrochemical performance. For the purpose of measuring the electrochemical performance of the prepared samples, a three-electrode electrochemical system was used. An aqueous solution of 1 M KOH was selected as the electrolyte solution. The polarization curves of all samples with *iR* corrected are shown as Figure 4a. The peaks around 1.38 V can be assigned to the oxidation of nickel species to a higher valence state. Furthermore, the $NiFe_2O_4/NiMoO_4$ demonstrates the lowest overpotential of 253 mV to reach 10 mA cm^{-2}, while the overpotential required to achieve 10 mA cm^{-2} for the NiFe PBA/$NiMoO_4$, $NiMoO_4$ O_2-Pl, $NiMoO_4$, and Ni foam is 310, 313, 324, and 431 mV, respectively. In addition, for the $NiFe_2O_4/NiMoO_4$, an overpotential of 270 and 309 mV are required to achieve 50 mA cm^{-2} and 500 mA cm^{-2}, respectively.

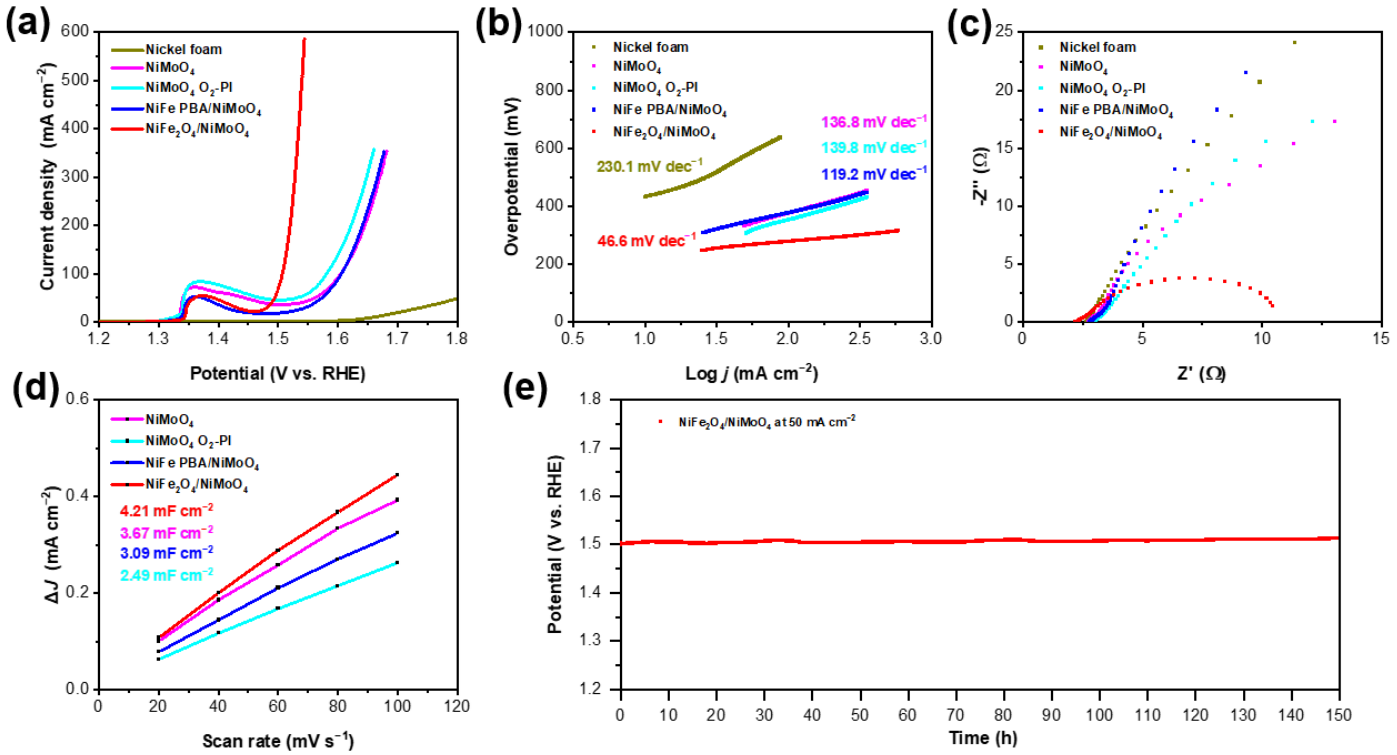

Figure 4. (**a**) Polarization curves and (**b**) corresponding Tafel slope plots of as-prepared catalysts; (**c**) EIS Nyquist plots of $NiMoO_4$, $NiMoO_4$ O_2-Pl, NiFe PBA/$NiMoO_4$, and $NiFe_2O_4$/$NiMoO_4$; (**d**) capacitive current densities plotted as a function of the scan rate; and (**e**) chronopotentiometry of $NiFe_2O_4$/$NiMoO_4$ at 50 mA cm^{-2} with *iR* corrected.

As shown in Figure 4b, the Tafel slope of the $NiFe_2O_4$/$NiMoO_4$ is the smallest, at 46.4 mV dec^{-1}, compared with that of the NiFe PBA/$NiMoO_4$ (119.2 mV dec^{-1}), $NiMoO_4$ O_2-Pl (139.8 mV dec^{-1}), $NiMoO_4$ (136.8 mV dec^{-1}), and Ni foam (230.1 mV dec^{-1}). The smaller Tafel slope of the $NiFe_2O_4$/$NiMoO_4$ indicates its faster kinetics [4,6]. The high performance of the $NiFe_2O_4$/$NiMoO_4$ can be attributed to the oxygen-plasma-induced formation of the hetero-interface, made up of $NiFe_2O_4$ NPs and $NiMoO_4$ nanowire arrays and containing iron with a higher valence. Iron with a higher valence has been confirmed to be conducive to the OER [54–57].

Figure 4c shows the electrochemical impedance spectroscopy (EIS) of all samples, and it can clearly be observed that the smallest charge transfer resistance (R_{ct}) is found in the $NiFe_2O_4$/$NiMoO_4$. The smaller R_{ct} relative to the others indicates a faster charge transfer for the $NiFe_2O_4$/$NiMoO_4$, which may relate to the hetero-interface made up of $NiFe_2O_4$ NPs and $NiMoO_4$ and further leads to enhanced electrocatalytic performance.

The electrochemical active surface area (ECSA) by CV measurement is shown in Figure S4. As shown in Figure 4d, the double-layer capacitance (C_{dl}) of the $NiFe_2O_4$/$NiMoO_4$, NiFe PBA/$NiMoO_4$, $NiMoO_4$ O_2-Pl, and $NiMoO_4$ was calculated to be 4.21, 3.09, 2.49, and 3.67 mF cm^{-2}. The larger value of C_{dl} indicates a higher electrocatalytic OER activity of the $NiFe_2O_4$/$NiMoO_4$, which is attributed to more exposed active sites related to the iron with a higher valence. Long-term stability is an important index for evaluating a catalyst. As shown in Figure 4e, the $NiFe_2O_4$/$NiMoO_4$ displays outstanding durability (a 4% increase in the overpotential at 50 mA cm^{-2} over a 150 h reaction).

In situ Raman spectra. To figure out the phase change and reconstruction in the OER process, the $NiFe_2O_4$/$NiMoO_4$ was first activated in an alkaline solution. In Figure 5a, with the increase in the applied potential from 1.18 V to 1.43 V, the intensity of characteristic peaks for Mo-O vibration decreased, which represents the dissolution of MoO_4^{2-}. Meanwhile, a small but sharp characteristic peak at 525 cm^{-1} corresponding with the Fe-O bond in FeOOH emerged with an applied potential of 1.23 V [58], which indicates the

formation of FeOOH in the OER process. When the potential is applied at 1.28 V, broad peaks can be observed around 460 cm^{-1} and 520 cm^{-1}, which are related to the appearance of α-$Ni(OH)_2$ [59]. The peak becomes sharper when the applied potential arrives at 1.33 V. A broad peak occurs at 475 cm^{-1}, which can be attributed to the emergence of γ-NiOOH from α-$Ni(OH)_2$ [32,58], and the peak tends to become sharper with an applied potential at 1.43 V, while another characteristic peak of γ-NiOOH appears at 558 cm^{-1} [32,59].

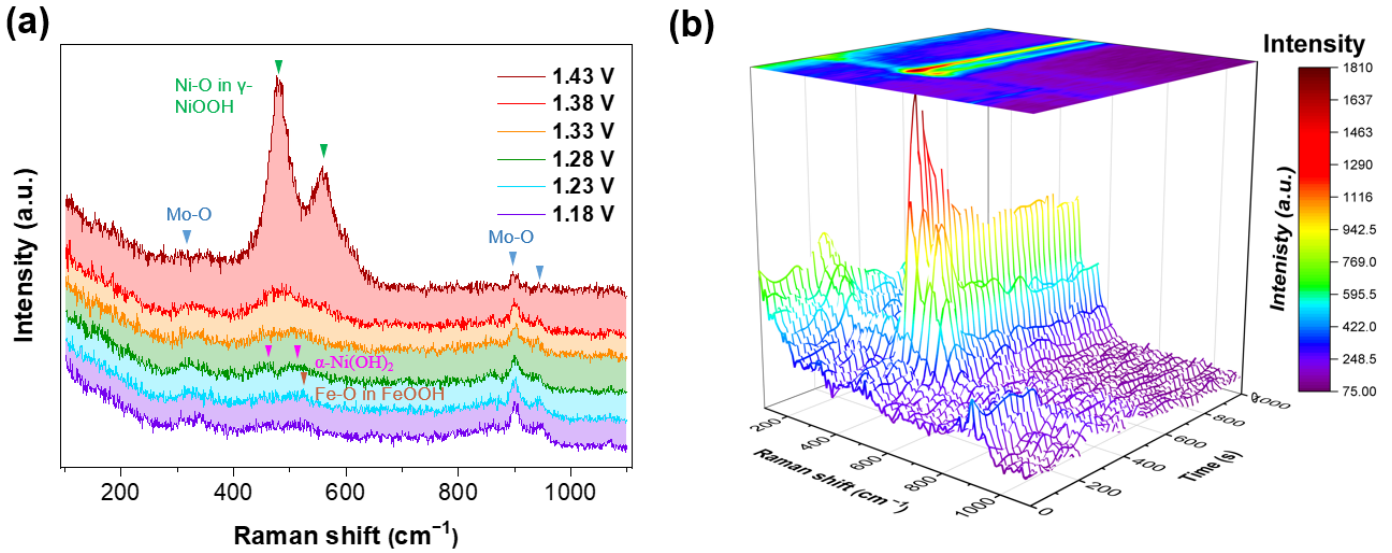

Figure 5. In situ Raman spectra of $NiFe_2O_4/NiMoO_4$ (**a**) for activation from 1.18 V to 1.43 V and (**b**) for CVs in the initial 2 cycles from 1.18 V to 1.43 V at a scan rate 1 mV s^{-1}.

In situ Raman spectra of the $NiFe_2O_4/NiMoO_4$ in the initial two cycles in CVs are shown in Figure 5b. With multiple cycles, the intensity of the characteristic peak for γ-NiOOH gradually stabilizes and the characteristic peaks of Mo-O vibration almost completely disappear, which can be attributed to the irreversible reconstruction of the $NiFe_2O_4/NiMoO_4$.

For comparison, the NiFe PBA/$NiMoO_4$ was also first activated in an alkaline solution. In Figure S8a, with the increase in applied potential, the same phenomenon of a decrease in the intensity of characteristic peaks for Mo-O vibration can be observed. In addition, when a potential of 1.38 V is applied to the $NiFe_2O_4/NiMoO_4$, a broad peak occurs at 475 cm^{-1}, which can be attributed to the emergence of γ-NiOOH. The same phenomenon occurs at an applied potential of 1.28 V for $NiFe_2O_4/NiMoO_4$. This fact means that the $NiFe_2O_4/NiMoO_4$ is reconstructed faster than the NiFe PBA/$NiMoO_4$, which leads to the better OER performance of the $NiFe_2O_4/NiMoO_4$ from another aspect. However, there are no observable peaks attributed to FeOOH, and in Figure S8b, with the increase in applied potential, the peaks related to -CN still exist [48,49]. This illustrates that the Fe coordinating with the cyanide group cannot catalyze the OER as an independent active site with the increase in applied potential, which further explains the reason that the OER performance of the NiFe PBA/$NiMoO_4$ is close to the OER performance of the $NiMoO_4$.

Ex situ XPS. The Ni 2p and Fe 2p spectra of the $NiFe_2O_4/NiMoO_4$ after 3 h of OER testing are shown in Figure 3d,e, respectively. In Figure 3d, the Ni 2p can be deconvoluted into two peaks with two satellites. The fitted peaks at 855.1 and 872.7 eV can be ascribed to Ni^{3+}, which is attributed to NiOOH [60]. Meanwhile, two satellites of Ni can be observed at 860.9 and 878.9 eV, respectively. As shown in Figure 3e, the two fitted peaks occur at 712.1 and 725.2 eV with a broad satellite at 718.3 eV, which can be related to FeOOH [61,62]. It can clearly be observed that there is a sharp attenuation in the peak intensity of the Mo 3d of the $NiFe_2O_4/NiMoO_4$ after 3 h of OER testing, further demonstrating the irreversible reconstruction of the $NiFe_2O_4/NiMoO_4$ with the dissolution of MoO_4^{2-}.

Ex situ TEM. The images of the $NiFe_2O_4/NiMoO_4$ after OER testing (Figure 6a,b) clearly show the robust surface of the nanowire and numerous defects as the result of the dissolution of MoO_4^{2-}. The HRTEM image in Figure 6c reveals clear lattice fringes of the (105) plane for NiOOH (JCPDF: 00-006-0075) with a crystalline interplanar spacing of 2.09 Å. The HRTEM image in Figure 3d shows small black particles distributed in clumps, which may relate to the amorphous FeOOH delivered by the activation of the $NiFe_2O_4$ in OER testing. The elemental mapping images (Figure 3e) indicate that Fe is still evenly distributed on the $NiMoO_4$ nanowire, and Mo dissolves in large quantities, which is consistent with the aforementioned analytical results.

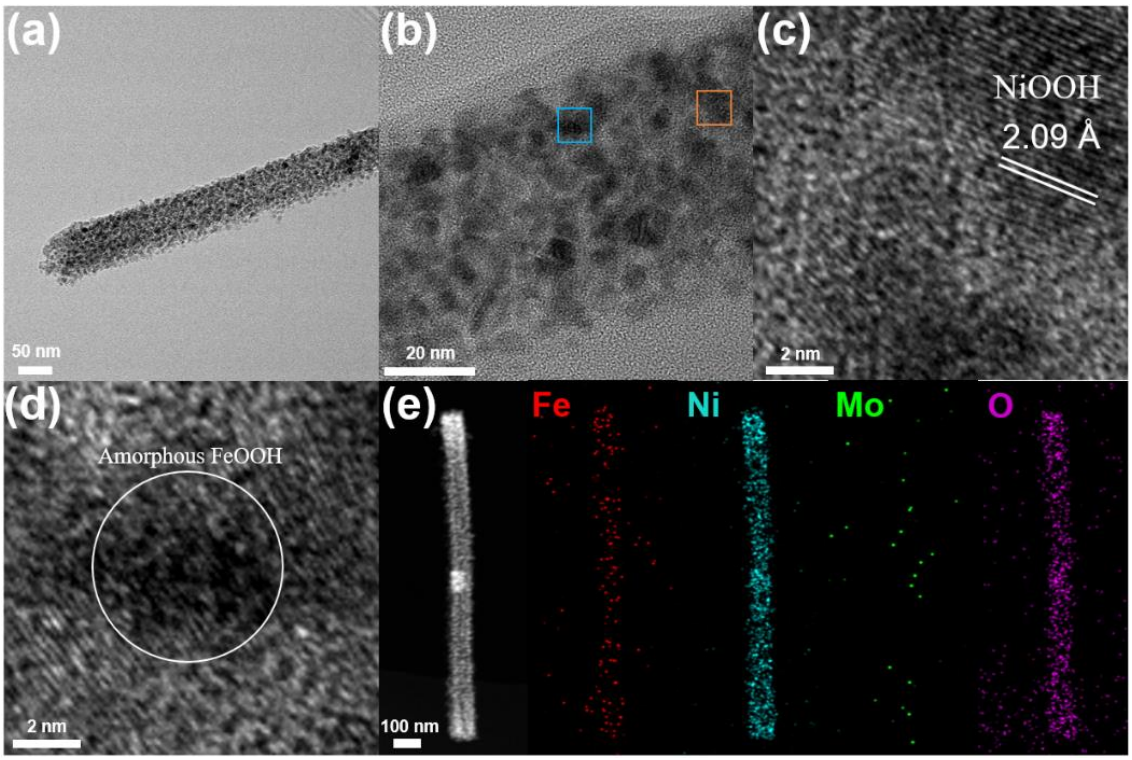

Figure 6. (**a**) TEM image; (**b**) HRTEM image of $NiFe_2O_4/NiMoO_4$ after 3 h of OER testing; (**c**) the corresponding HRTEM images of the area selected by the orange frame; (**d**) the corresponding HRTEM images of the area selected by the blue frame; and (**e**) EDS mapping images for Fe, Ni, Mo, and O elements of $NiFe_2O_4/NiMoO_4$ after OER.

3. Conclusions

In summary, a heterogeneous interface of $NiFe_2O_4/NiMoO_4$ with high-valence iron through oxygen plasma can be fabricated to achieve excellent electrocatalytic activity and stability. To achieve a current density of 50 mA cm^{-2}, 270 mV of overpotential is required, while an overpotential of 309 mV is required to reach 500 mA cm^{-2}. The $NiFe_2O_4/NiMoO_4$ also exhibits a satisfactory stability (a 4% increase in the overpotential at 50 mA cm^{-2} over 150 h). O_2-plasma-induced electronic interaction in the hetero-interface of $NiFe_2O_4/NiMoO_4$ and iron with a higher valence play an essential role in OER performance. The potential-dependent phase change and the fast and irreversible reconstruction of the $NiFe_2O_4/NiMoO_4$ in a catalytic process were identified by in situ Raman, ex situ XPS, and ex situ TEM measurements. Based on this, the true active species, NiOOH and FeOOH, were determined. This work provides a feasible design guideline for modifying electronic structure through the construction of a heterogeneous interface and the activation of metal sites by O_2 plasma, finally leading to enhanced OER performance.

Supplementary Materials: The following supporting information can be downloaded at: https://www.mdpi.com/article/10.3390/ma15103688/s1. Figure S1. SEM images (a, b) and (c, d) of $NiMoO_4$ and NiFe PBA/$NiMoO_4$, respectively. Figure S2. XRD patterns of NiFe PBA/$NiMoO_4$ and $NiFe_2O_4$/$NiMoO_4$. Figure S3. FT-IR spectra of $NiMoO_4$, NiFe PBA/$NiMoO_4$ and $NiFe_2O_4$/$NiMoO_4$. Figure S4. XPS spectrum of (a) $NiMoO_4$, $NiMoO_4$ O_2-Pl, NiFe PBA/$NiMoO_4$, $NiFe_2O_4$/$NiMoO_4$, and of (b) $NiFe_2O_4$/$NiMoO_4$ before OER and after OER. Figure S5. XPS (a) Ni 2p and (b) Fe 2p spectra of NiFe PBA/$NiMoO_4$. Figure S6. XPS analysis of NiFe PBA/$NiMoO_4$ and $NiFe_2O_4$/$NiMoO_4$. The core level spectra of (a) Ni $2p_{3/2}$ and (b) Mo 3d. Figure S7. Cyclic voltammograms in a capacitive current region at various scan rates from 20 to 100 mV s^{-1}. (a) $NiMoO_4$, (b) $NiMoO_4$ O_2-Pl, (c) NiFe PBA/$NiMoO_4$, (d) $NiFe_2O_4$/$NiMoO_4$. Figure S8. In situ Raman spectra of $NiFe_2O_4$/$NiMoO_4$for activation from 1.18 V to 1.63 V (a) in a region from 250 cm^{-1} to 1050 cm^{-1} and (b) in a region from 1500 cm^{-1} to 2500 cm^{-1}. Table S1. Chemical composition of $NiFe_2O_4$/$NiMoO_4$ based on EDS.

Author Contributions: Conceptualization, N.X. and W.P.; methodology, N.X.; software, L.L., P.X., C.W. and J.L.; validation, W.P.; formal analysis, N.X. and W.P.; investigation, N.X.; resources, N.X.; data curation, N.X.; writing—original draft preparation, N.X.; writing—review and editing, N.X.; visualization, W.L. and L.Z.; supervision, W.L. and L.Z.; project administration, W.L. and L.Z.; funding acquisition, W.L. and L.Z. All authors contributed to the critical literature review. All authors contributed to writing and revising the manuscript. All authors have read and agreed to the published version of the manuscript.

Funding: This work was supported by the National Natural Science Foundation of China (51904216, 21905218), the Natural Science Foundation of Hubei Province (2019CFA001), the Foshan Xianhu Laboratory of the Advanced Energy Science and Technology Guangdong Laboratory (XHT2020-003), and the Fundamental Research Funds for the Central Universities (WUT: 2020IVB034, 2020IVA036, 2021CG014). The TEM work was performed at the Nanostructure Research Center (NRC), which was supported by the Fundamental Research Funds for the Central Universities (WUT: 2019III012GX), the State Key Laboratory of Advanced Technology for Materials Synthesis and Processing.

Institutional Review Board Statement: Not applicable.

Informed Consent Statement: Not applicable.

Data Availability Statement: The data presented in this study are available from the corresponding author, upon reasonable request.

Conflicts of Interest: The authors declare no conflict of interest.

References

1. Chu, S.; Majumdar, A. Opportunities and Challenges for a Sustainable Energy Future. *Nature* **2012**, *488*, 294–303. [CrossRef] [PubMed]
2. Jiao, Y.; Zheng, Y.; Jaroniec, M.; Qiao, S.Z. Design of Electrocatalysts for Oxygen- and Hydrogen-Involving Energy Conversion Reactions. *Chem. Soc. Rev.* **2015**, *44*, 2060–2086. [CrossRef] [PubMed]
3. Li, L.; Wang, P.; Shao, Q.; Huang, X. Recent Progress in Advanced Electrocatalyst Design for Acidic Oxygen Evolution Reaction. *Adv. Mater.* **2021**, *33*, 2004243. [CrossRef] [PubMed]
4. Suen, N.T.; Hung, S.F.; Quan, Q.; Zhang, N.; Xu, Y.J.; Chen, H.M. Electrocatalysis for the Oxygen Evolution Reaction: Recent Development and Future Perspectives. *Chem. Soc. Rev.* **2017**, *46*, 337–365. [CrossRef]
5. Gao, L.; Cui, X.; Sewell, C.D.; Li, J.; Lin, Z. Recent Advances in Activating Surface Reconstruction for the High-Efficiency Oxygen Evolution Reaction. *Chem. Soc. Rev.* **2021**, *50*, 8428–8469. [CrossRef]
6. Li, S.; Gao, Y.; Li, N.; Ge, L.; Bu, X.; Feng, P. Transition Metal-Based Bimetallic Mofs and Mof-Derived Catalysts for Electrochemical Oxygen Evolution Reaction. *Energy Environ. Sci.* **2021**, *14*, 1897–1927. [CrossRef]
7. Song, J.; Wei, C.; Huang, Z.F.; Liu, C.; Zeng, L.; Wang, X.; Xu, Z.J. A Review on Fundamentals for Designing Oxygen Evolution Electrocatalysts. *Chem. Soc. Rev.* **2020**, *49*, 2196–2214. [CrossRef]
8. Zou, X.; Zhang, Y. Noble Metal-Free Hydrogen Evolution Catalysts for Water Splitting. *Chem. Soc. Rev.* **2015**, *44*, 5148–5180. [CrossRef]
9. Yan, D.; Li, Y.; Huo, J.; Chen, R.; Dai, L.; Wang, S. Defect Chemistry of Nonprecious-Metal Electrocatalysts for Oxygen Reactions. *Adv. Mater.* **2017**, *29*, 1606459. [CrossRef]
10. Shi, Y.; Zhang, B. Recent Advances in Transition Metal Phosphide Nanomaterials: Synthesis and Applications in Hydrogen Evolution Reaction. *Chem. Soc. Rev.* **2016**, *45*, 1529–1541. [CrossRef]

11. Su, X.; Wang, Y.; Zhou, J.; Gu, S.; Li, J.; Zhang, S. Operando Spectroscopic Identification of Active Sites in Nife Prussian Blue Analogues as Electrocatalysts: Activation of Oxygen Atoms for Oxygen Evolution Reaction. *J. Am. Chem. Soc.* **2018**, *140*, 11286–11292. [CrossRef] [PubMed]
12. Gao, Q.; Huang, C.Q.; Ju, Y.M.; Gao, M.R.; Liu, J.W.; An, D.; Cui, C.H.; Zheng, Y.R.; Li, W.X.; Yu, S.H. Phase-Selective Syntheses of Cobalt Telluride Nanofleeces for Efficient Oxygen Evolution Catalysts. *Angew. Chem. Int. Ed.* **2017**, *56*, 7769–7773. [CrossRef] [PubMed]
13. Li, S.; Chen, B.; Wang, Y.; Ye, M.Y.; van Aken, P.A.; Cheng, C.; Thomas, A. Oxygen-Evolving Catalytic Atoms on Metal Carbides. *Nat. Mater.* **2021**, *20*, 1240–1247. [CrossRef] [PubMed]
14. Aralekallu, S.; Sajjan, V.A.; Palanna, M.; CP, K.P.; Hojamberdiev, M.; Sannegowda, L.K. Ni foam-supported azo linkage cobalt phthalocyanine as an efficient electrocatalyst for oxygen evolution reaction. *J. Power Sources* **2020**, *449*, 227516. [CrossRef]
15. Duan, Y.; Yu, Z.Y.; Hu, S.J.; Zheng, X.S.; Zhang, C.T.; Ding, H.H.; Hu, B.C.; Fu, Q.Q.; Yu, Z.L.; Zheng, X.; et al. Scaled-up Synthesis of Amorphous Nifemo Oxides and Their Rapid Surface Reconstruction for Superior Oxygen Evolution Catalysis. *Angew. Chem. Int. Ed. Engl.* **2019**, *58*, 15772–15777. [CrossRef]
16. Kuznetsov, D.A.; Han, B.; Yu, Y.; Rao, R.R.; Hwang, J.; Román-Leshkov, Y.; Shao-Horn, Y. Tuning Redox Transitions Via Inductive Effect in Metal Oxides and Complexes, and Implications in Oxygen Electrocatalysis. *Joule* **2018**, *2*, 225–244. [CrossRef]
17. Li, J.; Chu, D.; Dong, H.; Baker, D.R.; Jiang, R. Boosted Oxygen Evolution Reactivity by Igniting Double Exchange Interaction in Spinel Oxides. *J. Am. Chem. Soc.* **2020**, *142*, 50–54. [CrossRef]
18. Zhou, J.; Zhang, L.; Huang, Y.C.; Dong, C.L.; Lin, H.J.; Chen, C.T.; Tjeng, L.H.; Hu, Z. Voltage- and Time-Dependent Valence State Transition in Cobalt Oxide Catalysts During the Oxygen Evolution Reaction. *Nat. Commun.* **2020**, *11*, 1984. [CrossRef]
19. Zhou, D.; Li, P.; Lin, X.; McKinley, A.; Kuang, Y.; Liu, W.; Lin, W.F.; Sun, X.; Duan, X. Layered Double Hydroxide-Based Electrocatalysts for the Oxygen Evolution Reaction: Identification and Tailoring of Active Sites, and Superaerophobic Nanoarray Electrode Assembly. *Chem. Soc. Rev.* **2021**, *50*, 8790–8817. [CrossRef]
20. Gao, M.; Sheng, W.; Zhuang, Z.; Fang, Q.; Gu, S.; Jiang, J.; Yan, Y. Efficient Water Oxidation Using Nanostructured α-Nickel-Hydroxide as an Electrocatalyst. *J. Am. Chem. Soc.* **2014**, *136*, 7077–7084. [CrossRef]
21. Yang, H.; Gong, L.; Wang, H.; Dong, C.; Wang, J.; Qi, K.; Liu, H.; Guo, X.; Xia, B.Y. Preparation of Nickel-Iron Hydroxides by Microorganism Corrosion for Efficient Oxygen Evolution. *Nat. Commun.* **2020**, *11*, 5075. [CrossRef] [PubMed]
22. Govind Rajan, A.; Martirez, J.M.P.; Carter, E.A. Facet-Independent Oxygen Evolution Activity of Pure Beta-Niooh: Different Chemistries Leading to Similar Overpotentials. *J. Am. Chem. Soc.* **2020**, *142*, 3600–3612. [CrossRef] [PubMed]
23. Ye, S.H.; Shi, Z.X.; Feng, J.X.; Tong, Y.X.; Li, G.R. Activating CoOOH Porous Nanosheet Arrays by Partial Iron Substitution for Efficient Oxygen Evolution Reaction. *Angew. Chem. Int. Ed.* **2018**, *57*, 2672–2676. [CrossRef] [PubMed]
24. Han, X.; Yu, C.; Zhou, S.; Zhao, C.; Huang, H.; Yang, J.; Liu, Z.; Zhao, J.; Qiu, J. Ultrasensitive Iron-Triggered Nanosized Fe-CoOOH Integrated with Graphene for Highly Efficient Oxygen Evolution. *Adv. Energy Mater.* **2017**, *7*, 1602148. [CrossRef]
25. Huang, Z.-F.; Song, J.; Du, Y.; Xi, S.; Dou, S.; Nsanzimana, J.M.V.; Wang, C.; Xu, Z.J.; Wang, X. Chemical and Structural Origin of Lattice Oxygen Oxidation in Co-Zn Oxyhydroxide Oxygen Evolution Electrocatalysts. *Nat. Energy* **2019**, *4*, 329–338. [CrossRef]
26. Sun, H.; Yan, Z.; Liu, F.; Xu, W.; Cheng, F.; Chen, J. Self-Supported Transition-Metal-Based Electrocatalysts for Hydrogen and Oxygen Evolution. *Adv. Mater.* **2020**, *32*, 1806326. [CrossRef]
27. Peugeot, A.; Creissen, C.E.; Karapinar, D.; Tran, H.N.; Schreiber, M.; Fontecave, M. Benchmarking of Oxygen Evolution Catalysts on Porous Nickel Supports. *Joule* **2021**, *5*, 1281–1300. [CrossRef]
28. Liu, Q.; Zhao, H.; Jiang, M.; Kang, Q.; Zhou, W.; Wang, P.; Zhou, F. Boron Enhances Oxygen Evolution Reaction Activity over Ni Foam-Supported Iron Boride Nanowires. *J. Mater. Chem. A* **2020**, *8*, 13638–13645. [CrossRef]
29. Li, R.-Q.; Wan, X.-Y.; Chen, B.-L.; Cao, R.-Y.; Ji, Q.-H.; Deng, J.; Qu, K.-G.; Wang, X.-B.; Zhu, Y.-C. Hierarchical $Ni_3N/Ni_{0.2}Mo_{0.8}N$ Heterostructure Nanorods Arrays as Efficient Electrocatalysts for Overall Water and Urea Electrolysis. *Chem. Eng. J.* **2021**, *409*, 128240. [CrossRef]
30. Wang, C.; Tian, Y.; Gu, Y.; Xue, K.-H.; Sun, H.; Miao, X.; Dai, L. Plasma-Induced Moieties Impart Super-Efficient Activity to Hydrogen Evolution Electrocatalysts. *Nano Energy* **2021**, *85*, 106030. [CrossRef]
31. Yin, Z.; Sun, Y.; Zhu, C.; Li, C.; Zhang, X.; Chen, Y. Bimetallic Ni-Mo Nitride Nanotubes as Highly Active and Stable Bifunctional Electrocatalysts for Full Water Splitting. *J. Mater. Chem. A* **2017**, *5*, 13648–13658. [CrossRef]
32. Durr, R.N.; Maltoni, P.; Tian, H.; Jousselme, B.; Hammarstrom, L.; Edvinsson, T. From $NiMoO_4$ to γ-NiOOH: Detecting the Active Catalyst Phase by Time Resolved in Situ and Operando Raman Spectroscopy. *ACS Nano* **2021**, *15*, 13504–13515. [CrossRef] [PubMed]
33. Wang, J.; Cui, W.; Liu, Q.; Xing, Z.; Asiri, A.M.; Sun, X. Recent Progress in Cobalt-Based Heterogeneous Catalysts for Electrochemical Water Splitting. *Adv. Mater.* **2016**, *28*, 215–230. [CrossRef] [PubMed]
34. Suryanto, B.H.R.; Wang, Y.; Hocking, R.K.; Adamson, W.; Zhao, C. Overall Electrochemical Splitting of Water at the Heterogeneous Interface of Nickel and Iron Oxide. *Nat. Commun.* **2019**, *10*, 5599. [CrossRef]
35. Guo, Y.; Yuan, P.; Zhang, J.; Xia, H.; Cheng, F.; Zhou, M.; Li, J.; Qiao, Y.; Mu, S.; Xu, Q. Co_2P-CoN Double Active Centers Confined in N-Doped Carbon Nanotube: Heterostructural Engineering for Trifunctional Catalysis toward Her, ORR, OER, and Zn-Air Batteries Driven Water Splitting. *Adv. Funct. Mater.* **2018**, *28*, 1805641. [CrossRef]

36. Wu, A.; Gu, Y.; Xie, Y.; Tian, C.; Yan, H.; Wang, D.; Zhang, X.; Cai, Z.; Fu, H. Effective Electrocatalytic Hydrogen Evolution in Neutral Medium Based on 2d MoP/MoS_2 Heterostructure Nanosheets. *ACS Appl. Mater. Interfaces* **2019**, *11*, 25986–25995. [CrossRef]
37. Lu, K.; Liu, Y.; Lin, F.; Cordova, I.A.; Gao, S.; Li, B.; Peng, B.; Xu, H.; Kaelin, J.; Coliz, D.; et al. Li_xNiO/Ni Heterostructure with Strong Basic Lattice Oxygen Enables Electrocatalytic Hydrogen Evolution with Pt-Like Activity. *J. Am. Chem. Soc.* **2020**, *142*, 12613–12619. [CrossRef]
38. Sun, J.; Xu, W.; Lv, C.; Zhang, L.; Shakouri, M.; Peng, Y.; Wang, Q.; Yang, X.; Yuan, D.; Huang, M.; et al. Co/MoN Hetero-Interface Nanoflake Array with Enhanced Water Dissociation Capability Achieves the Pt-Like Hydrogen Evolution Catalytic Performance. *Appl. Catal. B* **2021**, *286*, 119882. [CrossRef]
39. Lv, J.; Wang, L.; Li, R.; Zhang, K.; Zhao, D.; Li, Y.; Li, X.; Huang, X.; Wang, G. Constructing a Hetero-Interface Composed of Oxygen Vacancy-Enriched Co_3O_4 and Crystalline-Amorphous Nife-LDH for Oxygen Evolution Reaction. *ACS Catal.* **2021**, *11*, 14338–14351. [CrossRef]
40. Zhang, W.; Wang, Y.; Zheng, H.; Li, R.; Tang, Y.; Li, B.; Zhu, C.; You, L.; Gao, M.R.; Liu, Z.; et al. Embedding Ultrafine Metal Oxide Nanoparticles in Monolayered Metal-Organic Framework Nanosheets Enables Efficient Electrocatalytic Oxygen Evolution. *ACS Nano* **2020**, *14*, 1971–1981. [CrossRef]
41. CP, K.P.; Aralekallu, S.; Sajjan, V.A.; Palanna, M.; Kumar, S.; Sannegowda, L.K. Non-precious cobalt phthalocyanine-embedded iron ore electrocatalysts for hydrogen evolution reactions. *Sustain. Energy Fuels* **2021**, *5*, 1448–1457. [CrossRef]
42. Bai, L.; Lee, S.; Hu, X. Spectroscopic and Electrokinetic Evidence for a Bifunctional Mechanism of the Oxygen Evolution Reaction. *Angew. Chem. Int. Ed.* **2021**, *60*, 3095–3103. [CrossRef] [PubMed]
43. Clament Sagaya Selvam, N.; Kwak, S.J.; Choi, G.H.; Oh, M.J.; Kim, H.; Yoon, W.-S.; Lee, W.B.; Yoo, P.J. Unveiling the Impact of Fe Incorporation on Intrinsic Performance of Reconstructed Water Oxidation Electrocatalyst. *ACS Energy Lett.* **2021**, *6*, 4345–4354. [CrossRef]
44. Zhong, L.; Bao, Y.; Feng, L. Fe-Doping Effect on CoTe Catalyst with Greatly Boosted Intrinsic Activity for Electrochemical Oxygen Evolution Reaction. *Electrochim. Acta* **2019**, *321*, 134656. [CrossRef]
45. Guo, D.; Luo, Y.; Yu, X.; Li, Q.; Wang, T. High Performance $NiMoO_4$ Nanowires Supported on Carbon Cloth as Advanced Electrodes for Symmetric Supercapacitors. *Nano Energy* **2014**, *8*, 174–182. [CrossRef]
46. Choi, J.; Kim, D.; Zheng, W.; Yan, B.; Li, Y.; Lee, L.Y.S.; Piao, Y. Interface Engineered $NiFe_2O_{4-X}$/$NiMoO_4$ Nanowire Arrays for Electrochemical Oxygen Evolution. *Appl. Catal. B* **2021**, *286*, 119857. [CrossRef]
47. Xie, Y.; Chen, C.; Lu, X.; Luo, F.; Wang, C.; Alsaedi, A.; Hayat, T. Porous NiFe-Oxide Nanocubes Derived from Prussian Blue Analogue as Efficient Adsorbents for the Removal of Toxic Metal Ions and Organic Dyes. *J. Hazard. Mater.* **2019**, *379*, 120786. [CrossRef]
48. Wang, J.; Sun, M.; Wang, F.; Zhang, X.; Song, J.; Zhang, W.; Li, M. Essential Role of the Interfacial Interaction in the Core-Shell Electrode for Its Enhanced Electrochemical Performance. *Chem. Eng. J.* **2021**, *426*, 130895. [CrossRef]
49. Zhang, W.; Zhao, Y.; Malgras, V.; Ji, Q.; Jiang, D.; Qi, R.; Ariga, K.; Yamauchi, Y.; Liu, J.; Jiang, J.S.; et al. Synthesis of Monocrystalline Nanoframes of Prussian Blue Analogues by Controlled Preferential Etching. *Angew. Chem. Int. Ed.* **2016**, *55*, 8228–8234. [CrossRef]
50. Yilmaz, G.; Tan, C.F.; Lim, Y.-F.; Ho, G.W. Pseudomorphic Transformation of Interpenetrated Prussian Blue Analogs into Defective Nickel Iron Selenides for Enhanced Electrochemical and Photo-Electrochemical Water Splitting. *Adv. Energy Mater.* **2019**, *9*, 1802983. [CrossRef]
51. Ahmed, Z.; Krishankant; Rai, R.; Kumar, R.; Maruyama, T.; Bera, C.; Bagchi, V. Unraveling a Graphene Exfoliation Technique Analogy in the Making of Ultrathin Nickel-Iron Oxyhydroxides@Nickel Foam to Promote the OER. *ACS Appl. Mater. Interfaces* **2021**, *13*, 55281–55291. [CrossRef] [PubMed]
52. Das, D.; Santra, S.; Nanda, K.K. In Situ Fabrication of a Nickel/Molybdenum Carbide-Anchored N-Doped Graphene/Cnt Hybrid: An Efficient (Pre)Catalyst for OER and HER. *ACS Appl. Mater. Interfaces* **2018**, *10*, 35025–35038. [CrossRef] [PubMed]
53. Wu, Z.; Zou, Z.; Huang, J.; Gao, F. $NiFe_2O_4$ Nanoparticles/Nife Layered Double-Hydroxide Nanosheet Heterostructure Array for Efficient Overall Water Splitting at Large Current Densities. *ACS Appl. Mater. Interfaces* **2018**, *10*, 26283–26292. [CrossRef] [PubMed]
54. Chung, D.Y.; Lopes, P.P.; Farinazzo Bergamo Dias Martins, P.; He, H.; Kawaguchi, T.; Zapol, P.; You, H.; Tripkovic, D.; Strmcnik, D.; Zhu, Y.; et al. Dynamic Stability of Active Sites in Hydr(Oxy)Oxides for the Oxygen Evolution Reaction. *Nat. Energy* **2020**, *5*, 222–230. [CrossRef]
55. Zhang, B.; Wu, Z.; Shao, W.; Gao, Y.; Wang, W.; Ma, T.; Ma, L.; Li, S.; Cheng, C.; Zhao, C. Interfacial Atom-Substitution Engineered Transition-Metal Hydroxide Nanofibers with High-Valence Fe for Efficient Electrochemical Water Oxidation. *Angew. Chem. Int. Ed.* **2022**, *61*, 202115331.
56. Zhang, B.; Wang, L.; Cao, Z.; Kozlov, S.M.; García de Arquer, F.P.; Dinh, C.T.; Li, J.; Wang, Z.; Zheng, X.; Zhang, L.; et al. High-Valence Metals Improve Oxygen Evolution Reaction Performance by Modulating 3d Metal Oxidation Cycle Energetics. *Nat. Catal.* **2020**, *3*, 985–992. [CrossRef]
57. Lin, Y.C.; Chuang, C.H.; Hsiao, L.Y.; Yeh, M.H.; Ho, K.C. Oxygen Plasma Activation of Carbon Nanotubes-Interconnected Prussian Blue Analogue for Oxygen Evolution Reaction. *ACS Appl. Mater. Interfaces* **2020**, *12*, 42634–42643. [CrossRef]

58. Nieuwoudt, M.K.; Comins, J.D.; Cukrowski, I. The Growth of the Passive Film on Iron in 0.05 M NaOH Studied in Situ by Raman Micro-Spectroscopy and Electrochemical Polarisation. Part I: Near-Resonance Enhancement of the Raman Spectra of Iron Oxide and Oxyhydroxide Compounds. *J. Raman Spectrosc.* **2011**, *42*, 1335–1339. [CrossRef]
59. Lee, S.-Y.; Kim, I.-S.; Cho, H.-S.; Kim, C.-H.; Lee, Y.-K. Resolving Potential-Dependent Degradation of Electrodeposited $Ni(OH)_2$ Catalysts in Alkaline Oxygen Evolution Reaction (OER): In Situ XANES Studies. *Appl. Catal. B* **2021**, *284*, 119729. [CrossRef]
60. Mansour, A.; Melendres, C.J.S.S.S. Characterization of Electrochemically Prepared γ-NiOOH by XPS. *Surf. Sci. Spectra* **1994**, *3*, 271–278. [CrossRef]
61. Tan, B.J.; Klabunde, K.J.; Sherwood, P.M. X-ray Photoelectron Spectroscopy Studies of Solvated Metal Atom Dispersed Catalysts. Monometallic Iron and Bimetallic Iron-Cobalt Particles on Alumina. *Chem. Mater.* **1990**, *2*, 186–191. [CrossRef]
62. Welsh, I.D.; Sherwood, P.M.A. Photoemission and Electronic Structure of FeOOH: Distinguishing between Oxide and Oxyhydroxide. *Phys. Rev. B* **1989**, *40*, 6386. [CrossRef] [PubMed]